## Metals & corrosion

# Channelling electric current during the field-assisted sintering technique (FAST) to control microstructural evolution in Ti-6Al-4V

James Pepper[1],*[ID], Oliver Levano Blanch[1], Ben Thomas[1], and Martin Jackson[1]

[1] Department of Materials Science and Engineering, University of Sheffield, Sir Robert Hadfield Building, Mappin St, Sheffield S1 3JD, UK

## ABSTRACT

Perhaps the most defining feature of field-assisted sintering technology (FAST) is the application of an electric current, in addition to the uniaxial pressure, to create resistive heating in and around the sample region. However, with a few exceptions, most research takes this as an unchangeable part of the process. Here, this current flow has been directed to specific regions within the toolset, using boron nitride as electrically insulating material. This caused the heating to occur in differing regions within the Ti-6Al-4V sample and mould over four insulating configurations, with the shift in current density resulting in an extreme disparity in the final microstructures. The samples were imaged and analysed with deep learning in MIPAR, alongside comparisons with finite element analysis (FEA) models for 20 s and 5 min dwell times, to provide the technique with predictive capabilities for grain size and microstructure. The results gathered imply significant potential for this concept to improve the flexibility of FAST, and reduce negative effects such as undesirable temperature profiles in size scaling sintering for industry.

## Introduction

Powder consolidation is a diverse field, full of potential. However, with this potential comes a slew of problems and limitations associated with each of the varied techniques. Currently, one of the most promising solid-state process variants is field-assisted sintering technology (FAST), also known as spark plasma sintering (SPS). FAST is capable of consolidating a wide variety of powder materials from ceramics [1, 2] to composites [3], as well as many metallic systems [4–6]. Through resistive heating, this process can generate fully dense samples at a range of temperatures allowing for some degree of control in microstructural evolution, and thus, mechanical properties. Additionally, FAST performs this process many times faster than other alternative techniques such as hot isostatic pressing (HIP) [7]. This increase in speed and efficiency comes from

---

Handling Editor: David Cann.

Address correspondence to E-mail: jgpepper1@sheffield.ac.uk

the simultaneous application of high uniaxial pressure, and temperature via Joule resistive heating from pulsed current passing through the graphite tools and materials to be sintered. The technique is also capable of much higher heating rates than other high pressure methods at 200 °C per min for this machine, or up to 600 °C per min in some cases [8].

This low-voltage, DC-activated, synthesis and sintering technique has used this applied uniaxial pressure, in conjunction with resistive heating, to consolidate a wide variety of materials since its inception. Though it has a relatively short history, with much of the work since its patenting in the 1960 s focusing on its ability to rapidly sinter materials which are otherwise challenging to consolidate, such as ceramics or refractory materials. Over the last decade, it has gained popularity as a technique, becoming the sintering method of choice in several of these fields. However, until recently, very little work has investigated the potential to spatially fine-tune the most unique factor of this process, the electric current and resulting heating. Zapatas [9], and Geuntak et al. [10] used alumina fibres, borosilicate, and boron nitride, respectively, as insulators to completely isolate the sample from current, or to ensure that nearly all of the current flows through the sample in their work. Additionally, Manière et al. used an expansion of this concept in his work on nickel alloys [11, 12] with a "controllable interface method" in an attempt to channel the current through more conductive graphite foil regions for shaped production.

In this work, it is attempted to further advance this concept using high-strength, lightweight aerospace titanium. Ti-6Al-4V powder was chosen here, due to its excellent properties [13–15] for real-world applications such as aerospace engines medical implants or tools. It is these diverse and impactful uses driving the recent rising popularity in the field [16]. Titanium alloys also commonly possess a microstructural sensitivity at specific temperatures which aids in analysing the resulting temperature profiles. This change falls between the two allotropes of titanium, the $\alpha$ phase of hexagonal close-packed structure, and the $\beta$ phase above 994 °C for Ti-6Al-4V which is body-centred cubic. Although much of this structural change reverts upon cooling to the $\alpha$ phase, it leaves prior $\beta$ regions which have experienced much greater grain growth during heating than their $\alpha$ stable counterparts. It is with these larger prior $\beta$ grains, that this work aims to quantitatively determine the impact of the thermal

gradients along with the more qualitative "$\beta$ transus line", where the boundary between grains which did and did not experience this allotropic change can be seen.

These alloys are also currently expensive and difficult to produce, making the flexibility and control FAST offers incredibly appealing [17, 18], with large potential reduction in costs and little loss in component complexity appealing even further. Current limitations in the production cost for titanium components [19] have driven a wave of interest for a "right first time" approach where the component is created in the minimum number of steps possible to reduce the price and the number of costly machining steps. With the ideal for FAST processing of titanium being this "right first time" approach, the flexibility and control of the technique become more important, as each further machining or thermomechanical processing step required will reduce the benefits provided by the technique.

The primary goal is to investigate the potential of further shaping the current profile with tailored boron nitride (BN) shapes applied to the graphite foils connecting a sample to the wear pads, as shown in Figs. 1 and Fig. 2. Boron nitride was chosen due to its nature as a cheap and readily available material providing good potential for industry use. It is also capable of maintaining the insulating properties required at the high temperatures present in the titanium sintering process. As mentioned, the current is an important aspect of the FAST process, with the direct pulsed current providing the control and exceptional heating rate which make it unique amongst similar techniques, such as HIP. However, there are still aspects of this mechanism whose impact on the process is less well-understood, such as surface cleaning [20] and potential arcing or plasma sparking between particles [21] during the early stages of sintering. It is hoped that by furthering understanding of this current channelling approach it will provide more control of microstructural properties, thus leading to more efficient use of material. With this, new options will become available to industry, and the accompanying analytical process may also prove beneficial to other fields.

In all samples where BN is involved, the connection to the mould is insulated to ensure that the path of least resistance available to the current will be created where possible. A fully insulated design was also included to determine another end parameter to this design process and any parallel vs perpendicular
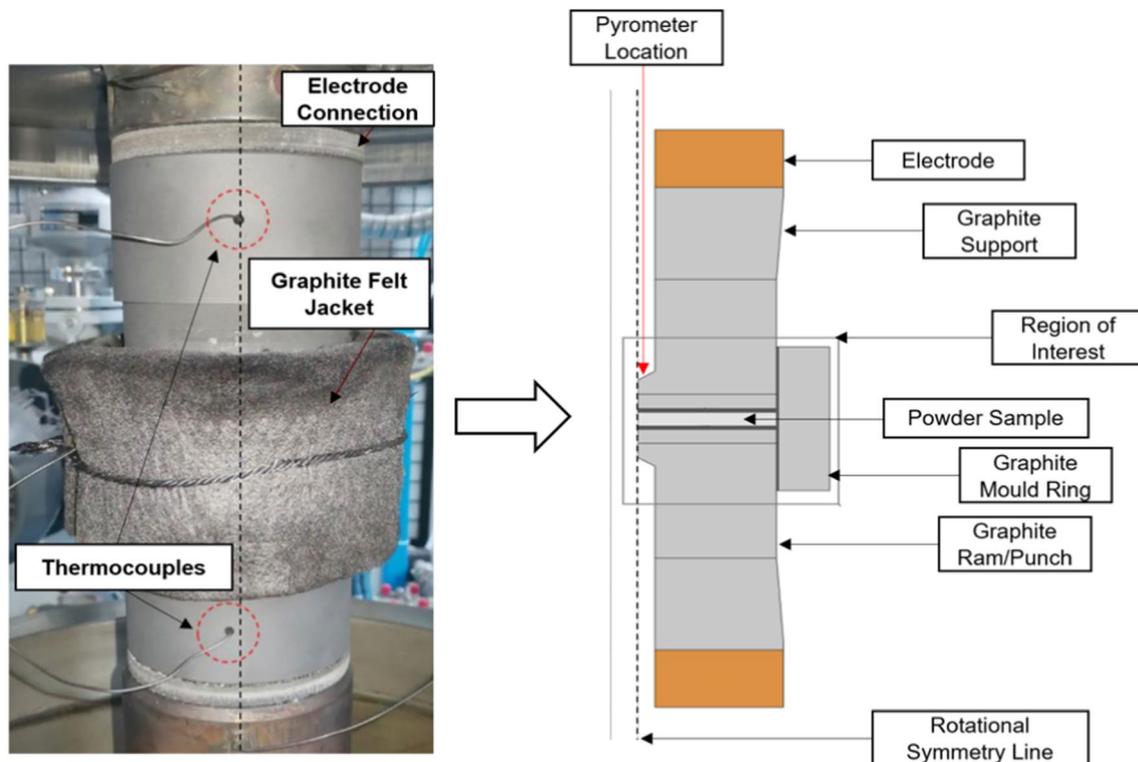
**Figure 1** Left: Photograph of 80-mm graphite tooling in the FAST vacuum chamber/Left: Labelled schematic of the 2D uni-axial slice of the FAST tooling stack. The location of measure-ment for the optical pyrometer and rotational axis of the 2D axial symmetry are also labelled here.

effects in this additional resistance to the foils [22]. These designs were formulated using a finite element analysis (FEA) model to predict the current density and how this in turn would impact the temperature profile during the sintering process. Designs were chosen based on two major factors, firstly that they produced a temperature profile which was sufficiently intense to be perceived practically, and secondly that the resolution of the design was large enough to allow current to pass through the uninsulated spaces unimpeded where desired. Figure 3 demonstrates this effect from experimentally covering a 20-mm-diameter circle of this material with BN, providing a framework to experiment within.

The reason for turning to this FEA technique is that the physical system within the FAST machine is a complicated "black box" which may only be indirectly measured without impacting the results. This is to say that although many macro- and micro-mechanisms have been proposed to explain the densification process of the powder [23, 24], the state of the sintered sample cannot easily be directly observed during the process. In terms of the sintering densification, many

studies and models have been proposed to probe into this "black box" within the tooling [25, 26]. These primarily discuss the correlations of shrinkage behaviour, densification mechanisms, and atomic diffusivity, linking these to theoretical frameworks and thus models of the process.

Multiple of these physical models have been proposed to discuss the densification process and many have been backed by calibrated experimental results [27], though the complexities and variations between powders and machines provide additional complications. For titanium alloys such as Ti-6Al-4V investigated here, necking from grain boundaries, volume and surface diffusion, are the primary early consolidation processes, and the high temperatures involved in FAST provide more kinetic energy for these processes to occur [28], depending on powder morphology. Combining bulk and surface atomic mobility on the micro-scale with void evolution and shrinkage on the macro-scale, at later sintering stages, is a multi-scale computational challenge facing the field to this day. Because of this, the densification mechanisms of multi-physics field sintering processes are not thoroughly understood, and these
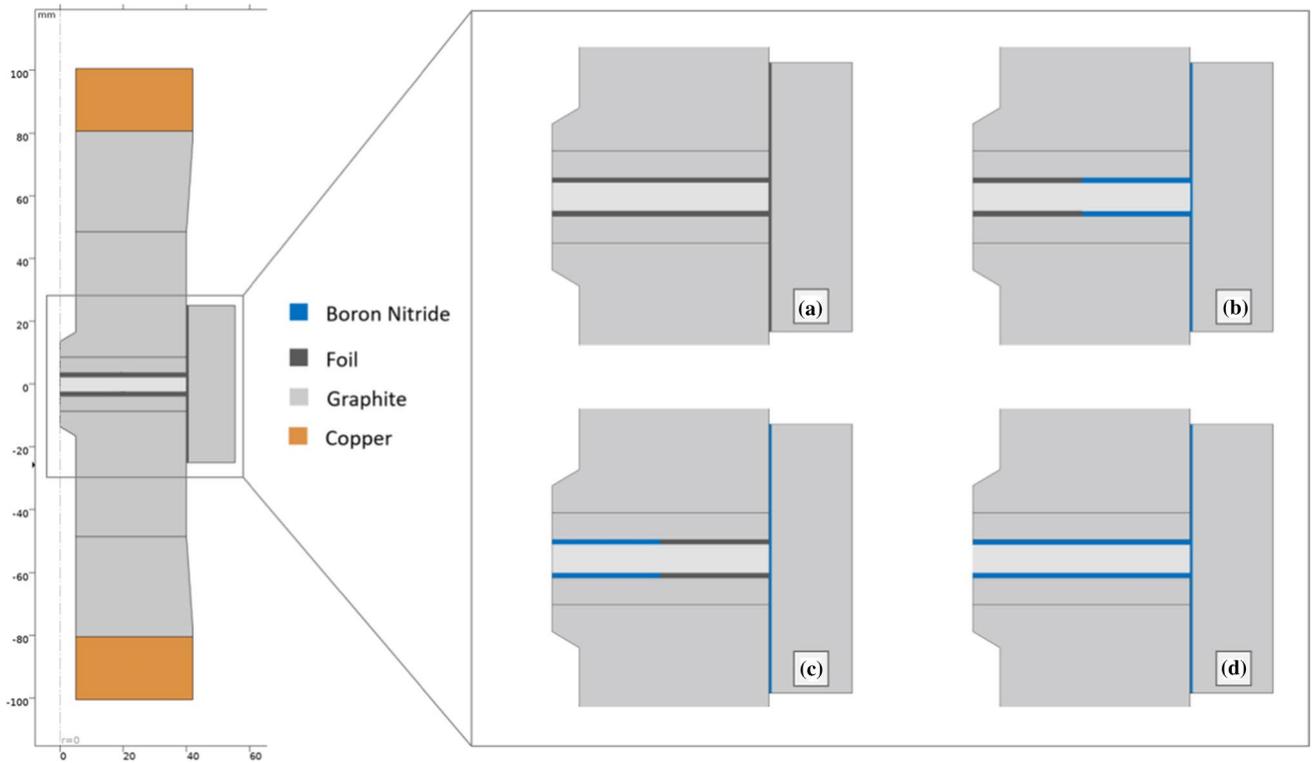
**Figure 2** Left: Simplified 2D uniaxial slice of the simulated 80-mm graphite tooling stack. The primary region of interest highlighted and enlarged, showing placement of the BN-coated graphite foil layers for insulation in blue. Right: A-Control | B-Aperture | C-Reverse Aperture | D-Full Insulation.

**Figure 3** Plots demonstrating the rise in resistance to the normal flowing current as the surface % of graphite foil coated with boron nitride (A) increases. For circles with approximately 85% or higher coverage, there was a sharp increase in total resistance. This was noticeably larger for thicker coatings of the insulator with six layers registering as almost three times as resistive as 3.
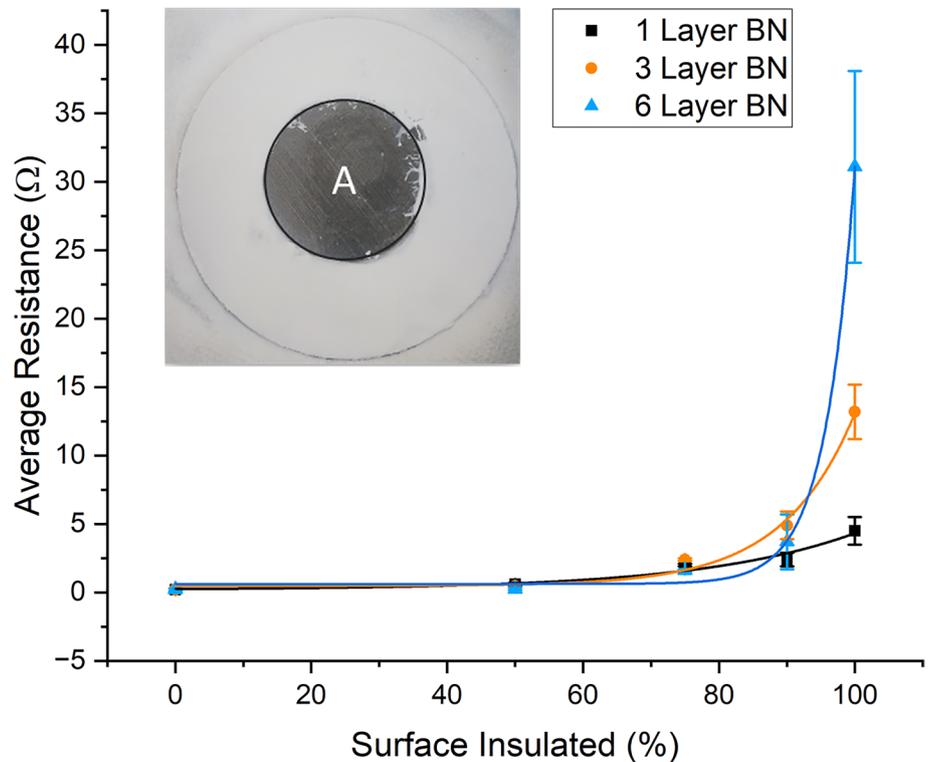
**Table 1** Graphite material property results from two isostatically moulded graphite grades tested, used in the production of sintering tooling. Thermal conductivity, specific heat capacity, and electrical conductivity are recorded at room temperature (RT) but were also gathered with temperature dependency for further accuracy. The coefficient of thermal expansion was also taken and recorded as a temperature-dependent function to be included in the simulations

| Test | Y-552 | Y-542 |
| --- | --- | --- |
| Compression strength − 0.1 s | 157.3 ± 4.2 MPa | 101.5 ± 2 MPa |
| Compression strength − 0.01 s | 155.6 ± 1.6 MPa | 98.2 ± 0.4 MPa |
| Flexural strength | 44.1 ± 1.4 MPa | 30.6 ± 0.7 MPa |
| Electrical conductivity (RT) | 6.3E +04 ± 355.9 S/m | 7.3E +04 ± 805.5 S/m |
| Thermal conductivity (RT) | 107.2 ± 1.1 W/(m.K) | 140.5 ± 3.2 W/(m.K) |
| Specific heat capacity (RT) | 0.7 ± 0.1 J/(g.K) | 0.68± 0.2 J/(g.K) |

simulations combined with the deep learning image analysis concept proposed in this work become more relevant and impactful for exploring them.

As an additional complexity, the sample temperature may only be measured using an external pyrometer or thermocouple, which has potential to record a different temperature due to the thermal profiles, or heat lag in the system. As such, it would be challenging to design a surface insulation pattern to direct the current to achieve the desired result without much trial and error, reducing the "right first time" impact of the concept. Therefore, a finite element model (FEM) was chosen to be used in parallel to the sample creations to act as a pseudo-digital twin of the FAST process through COMSOL [21, 29], allowing understanding of the impacts of the insulation on the current and therefore the temperature profiles. From this knowledge, it is also hoped to be able to predict the eventual microstructures and densities based on understanding of the alloys in question.

It is the hypothesis here that this targeted current channelling technique will provide a greater concentration of current and therefore a more significant temperature increase in regions left uninsulated, resulting in greater densification and grain growth for short dwell FAST processing. Longer dwell processing is also possible and will be examined in future works when specific tooling can be designed and tested for purpose.

## Methods

### FEM simulation

This simulation relies on three interlinked primary physical systems, resulting in coupled thermal, electrical, and solid mechanical calculations needing to be performed and linked for each step. Iterative calculations, such as those involved in the discrete element method, regard the sintered particles as independent, which on this scale prohibit computationally intense multi particle approaches [30, 31], necessitating a powder modelling approach. For the purposes of this work, a model representing the near consolidated state during dwell was sufficient in order to examine the equilibrated thermal gradients in the samples. During these numerical simulations, ohmic resistive heating is the main focus, as well as the impact on energetic development of titanium and resulting microstructure.

All FEM simulations were performed in COMSOL Multiphysics software Ver 5.6[32, 33] and used a 2D axisymmetric approach to further simplify the computational requirements commonly used in similar work [34, 35] (demonstrated in Fig. 2). These simulations used the resistance results from Fig. 3 as boundary conditions to input the effect of BN insulation on current flow and density. Remaining contact boundary conditions were defined using data presented in work from Manière et al. [36], and graphite–titanium boundaries are assumed as ideal graphite–graphite

contact due to the addition of foil in the sample creation. A dataset for the graphite tooling materials collected for Olmec Advanced Materials grades Y-552 and Y-542, Fig. 1, was utilised to generate a more accurate set of insulation profiles for the machine in this study, though literature values were used for the titanium sample. Surface effects are assumed entirely radiative with an emissivity of 0.8 approximating the near vacuum state in the machine. This heat loss is accounted for in COMSOL where $q$ is the heat flux per area $v$ is emissivity and $\xi$ is the Stefan–Boltzmann constant:

$$q_r = v\xi(T_w^4 - T_0^4) \tag{1}$$

All physical partial differential equation (PDE) calculations were handled within the simulation using COMSOL's Multiphysics package, allowing for the efficient generation of data for design and prediction of samples. Dynamic elastic motion and electrical potential can reach the equilibrium state in a much shorter time frame with the heat transfer, so mechanical and electric factors are considered to be quasi-static to further reduce the models complex nature. The DC current is set to be unpulsed for the purposes of simplicity, and the resulting electromagnetic heating is governed by the following PDE within the package:

$$\rho c_p \frac{\delta T}{\delta t} + \rho c_p u \cdot \nabla T = \nabla \cdot (k\nabla T) + Q_e \tag{2}$$

The current providing this heating in the model is determined using a proportional-integral-derivative (PID) controller similar to the physical machine with feedback from the previous iterations. Impact on current delivery is dependent on the desired heating profile and pyrometer temperature readings, and is inputted as a normal current density through the face of an electrode. Edge temperatures of these electrodes were fixed at room temperature to emulate the efficient liquid cooling they experience, although the practical temperatures vary by a few degrees depending on power load. Finally, while the solid mechanics in the simulation are included as a pressing force through the top ram, they have relatively little impact on the heating profiles of interest. This is due to the primary focus being the near consolidated dwell region of the sintering runs with a focus on final height microstructure (Table 1).

## Resistance measurements

Before the samples were created, an accurate series of measurements were taken using a sample resistivity test unit from the *Lotus Engineering Instrumentation Department*[tm] to gain an understanding of the resistivity of the graphite foils when coated with layers of BN. 20-mm-diameter foils were cut and tested with 1, 3, and 6 coatings in total. Readings were taken 5 times on separately prepared foils and averaged to account for marginal differences in thickness. A region of the foil was left uncoated for the readings between 0 and 100% surface foil coverage of the insulation spray. This resistance testing covered samples with 100, 90, 75, 50, and 0% BN surface coverage of the circular foils, which were then tested.

It was noted that the effectiveness of insulation falls rapidly as the surface is exposed, losing 90% of its total effect after exposing only 15–20% of the surface. With an exposed circle of graphite foil 10-mm diameter centred on the foil, 75% coverage was achieved. At this level of coating, there was a significant increase in conductivity when compared with full surface covering, clear in Fig. 3, and not much lower than the base conductivity of the foil itself. This implies that a majority of the current is now being channelled through the exposed aperture rather than evenly across the surface, a theoretical fourfold increase in current density for a 25% aperture in the central region of the sample. This would make for very efficient heating for targeted regions within a sample.

## Sample creation

To create the samples to compare with simulated results, commercially available Ti-6Al-4V Puris[tm] blend Bl-067 powder, within ASTM grade 5 specifications, with reported particle D50 of 163 $\mu$m was used. However, for rigour, a more specific size was determined using a Malvern Mastersizer 3000 laser diffraction particle size analyser with a wet dispersion method. A total of 3 repetitions were conducted to confirm previous results where this powder had been previously tested [37]. The D10-D90 scale was shown to be between 92–297 $\mu$m (Fig. 4), within error of the previously recorded results. The powder was poured into moulds of Y-552 graphite from Olmec Advanced Materials for sintering by hand after weighing a fixed quantity to achieve a predetermined final height of 11–12 mm.
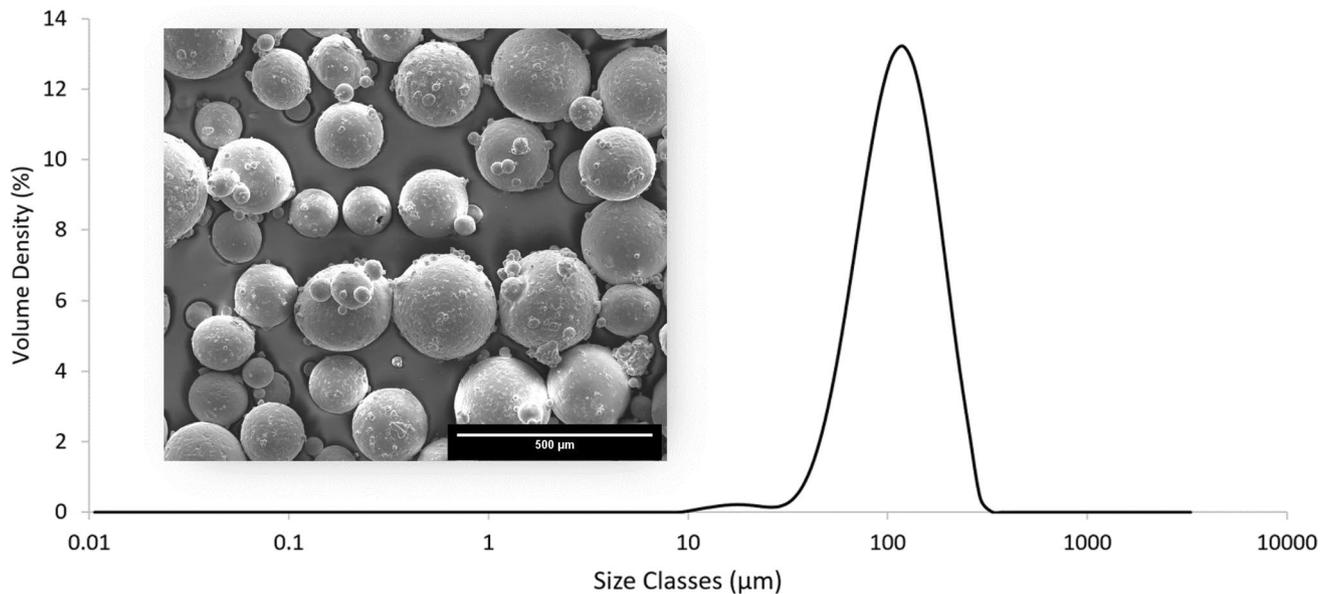
**Figure 4** Our Ti-6Al-4V Puris Powder Size Distribution (PSD) as measured on the Mastersizer 3000, averaged over several runs with inset Inspect F50 sary Electron Micrograph image (20 kV accelerating voltage) of the powder's topography and sphericity.

For the preparation of the samples for sintering, six layers of BN spray were applied to 0.35-mm-thick graphite foils, three per side. The primary use of this foil is to create electrically conductive contacts between the sample and tooling material. However, these foils were sprayed with BN through templates to block the spray for prescribed regions, shaping the resulting coating. A control was implemented with no insulation, and one sample which had all graphite foils coated to 100%, with the aim of exemplifying extreme insulation effects. For the intermediate, partially insulated designs, it was decided to focus the heating at the centre and edge, respectively, by attempting to direct current through these regions of the sample. All samples were then assembled with the graphite tooling and powders and pre-pressed at 0.6 kN before being pressed to 16 kN (32.5 MPa) over 5 min and only subsequently heated at a rate of 200 °C per minute to 1015°C. This temperature was chosen to allow for sufficient time above the $\beta$ transus of the titanium alloy with short dwell times to allow noticeable prior $\beta$ grain growth, while remaining low enough for the differences in grain size and $\alpha/\beta$ morphology to be determined visually. The FAST sintering machine used a pulsed current application of 15 ms on and 5 ms off DC current for easier comparison with previous work performed and for better consolidation. To prevent unnecessary oxidation of the Ti-6Al-4V powder,

the process is carried out under vacuum, which is confirmed and controlled with an internal system to $10^{-3}$ bar. When at temperature, they were held for 0 s, and 5 min of dwell for each insulating pattern. They were then allowed to cool freely under the same vacuum and removed from the graphite moulds.

The sintering itself was performed in a *FCT Systeme GmbH Spark Plasma Sintering Furnace type HP D 25* and monitored with a pyrometer monitoring the temperature within a hollow ram. The internal diameter of the graphite ring was 80 mm, and no external thermal insulating material was included. Samples were then sectioned, mounted in conductive carbon filled Poly-Fast$^{tm}$ Bakelite, ground, polished, and etched in Kroll's reagent (*HF* 2%, *HNO* 6%, $H_2O$ 92%) for 15–20 s before cleaning to check and reveal the grain structure. A Struers Tegramin−25 was used for grinding/polishing, and the surfaces were ground for 2 min using P800, P1200, and P2500 *SiC* grit papers, followed by polishing with a 9-part 0.06-$\mu$m colloidal silica and 1-part hydrogen peroxide suspension for 10 min.

Using the *Olympus$^{tm}$ BX51* microscope, optical micrograph mosaics were taken from two slices of half the surface at 100x magnification with a compensated overlap. Focusing was determined using a plane of focus created prior to imaging, which was performed with a spatial resolution of 1.094 $\mu$m/pixel. This imaging was performed using *Clemex$^{tm}$* software and an

**Table 2** Data comparison between experimental runs and associated models demonstrating a 2–6% match on the current and voltages with a remarkable 1–2% match for the resistances. This implies a marginal error arising from the simulation simplifications made. However, it was decided that this was sufficiently accurate for the validations

| | I (kA) | I Sim (kA) | Diff % | V (V) | V Sim (V) | Diff % | Res (kΩ) | Res Sim (kΩ) | Diff % |
|---|---|---|---|---|---|---|---|---|---|
| Control | 5.24 | 5.55 | 5.92 | 5.22 | 5.50 | 5.31 | 0.997 | 0.991 | 0.57 |
| Aperture | 3.71 | 3.50 | 5.79 | 5.49 | 5.20 | 5.28 | 1.478 | 1.486 | 0.53 |
| Reverse | 4.33 | 4.50 | 4.02 | 5.04 | 5.14 | 2.04 | 1.164 | 1.142 | 1.91 |
| Full | 3.68 | 3.45 | 6.27 | 5.47 | 5.15 | 5.77 | 1.485 | 1.493 | 0.53 |

automated stage to acquire images across the whole sample surface.

## Image analysis methods

These micrographs were analysed in Materials Image Processing and Automated Reconstruction software (MIPAR$^{tm}$) [38–40] to determine both the average grain size and the distribution to be related to the processing temperature. To perform the analysis of these grains in the software, grain boundaries were drawn manually on top of 50 reference images, taken from the samples in question, and used to train a "Deep Learning" algorithm to recognise these grain boundaries under the lighting and magnification conditions used to capture sample micrographs. This was used as part of a recipe to then identify grains within further micrographs, the first step of which is the deep learning model using techniques such as semantic segmentation to identify the prior $\beta$ grain boundaries and improved with a variety of other inbuilt commands. Any which did not have a complete boundary due to a connection with the image edge were then discounted to minimise errors in under-measuring as well as overcounting, and an average was taken for each image.

## Results and discussion

The findings must first be discussed with reference to the electro-thermal-mechanical simulations used to design them. These, as with most simulations, required validation through comparison to experimental results. The first aspect of the FEA technique which needed thorough analysis was the mesh used. This was put through a refinement process where a series of stable mesh configurations within the COMSOL software were parametrically swept, while all other parameters were kept constant for each simulation. It was found that this can have as much as a 5% potential impact on temperature readings if not optimised, with values dependent on the mesh scale in the sample region relative to the convergence point. However, using the smallest possible mesh to reach this convergence point exactly is wasteful computationally, and this value was reasonably reached with a maximum element size of 11 for the models. To optimise performance, increasing the computational requirements by further refining this mesh was seen as irrelevant and so these were the parameters used.

When the simulation was compared thermally at the pyrometer location, and electrically through both the current (I rms) and voltage across the simulated section of tooling, the accuracy was very good. These results from Table 2 show a strong correlation with the practically acquired results, with low average % deviation in the region of interest. It was expected that the temperature recorded at the pyrometer location follows the planned profile for heating as this was the PID feedback condition for the model and as such has not been included having a maximum error of 0.5 % in this region. However, the current and voltage also showed good agreement, and thermocouple data also previously demonstrated a qualitatively strong connection. It is believed that this is sufficient to have demonstrated the validity and accuracy of the simulation for obtaining the thermal profiles desired.

The simulated predictions for the thermal distributions which can be seen in Fig. 5 (A–D) demonstrate the impact of current density redistribution at the otherwise stable sintering dwell phase. With temperature differences of greater than 100°C over the radius of some samples, 40 mm across, processing at temperatures around the $\beta$ transus point, as is done here, could have a single sample demonstrating the full transition from sub- to super-transus microstructure. It is also clear from the results that while there is some small change in the thermal profile early in the dwell, it does
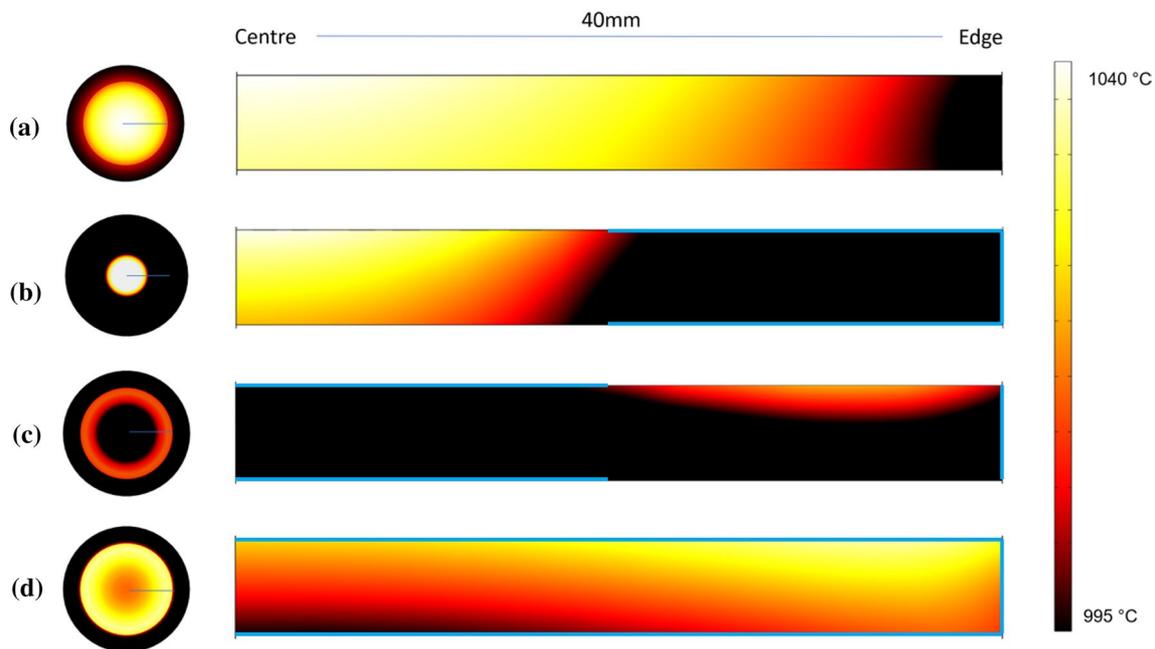
**Figure 5** Left—Temperature cross sections taken from the simulated region of interest at maximum temperature for each of the insulation configurations. Sample radius noted by the blue line. Right—2D axisymmetric display of the sample regions thermal distributions in both X and Y. Minimum temperature displayed is 994°C as the transus condition for this titanium alloy. (A-Control, B-Aperture, C-Reverse Aperture, D-Full). For clarity, BN regions are once again highlighted in blue.

not change the overall profile significantly. It is however likely that at these temperatures, the BN's loss of resistivity with extended exposure to heat would have some significant impact on runs with longer dwell times. For cases such as these, a potentially different method of insulation would be recommended, such as alumina tooling or similarly electrically insulating materials.

## Image analysis

To analyse the samples and provide an analytical determination of the thermal profiles impact, MIPAR was selected. Though occasionally imperfect in its determination of grain boundaries, it was determined visually that very few of the resulting images were significantly misaligned with the underlying grains. Between this and a Gaussian "blurring" technique to visualise trends, it was believed that the results were more than accurate enough to report here, and further improvement in the recipe may be possible during future work.

The samples with a dwell time of 20 s were a snapshot of the very early process with regions of sub- and super-transus clearly visible upon etching certain samples, (see Fig. 6). However, after later processing with MIPAR, it was found that there was no major region where the prior $\beta$ average grain diameter was differentiated by more than 20 $\mu m$. This was expected to some degree as there was not enough time above the $\beta$ transus for the grains to grow significantly. Though now with this quantitative knowledge, a timeline to the growth of these super-transus grains can be provided in relation to their applied temperature. Given the size of grains that were observed, there was some correlation to that of the initial powder size, demonstrating that with limited time post-consolidation, the microstructure is "penned in" by the initial powder size in the early stages of sintering and must be considered in future trials.

### Characterisation

In some samples, once etched, a clear boundary exists between regions of the sample that were above the
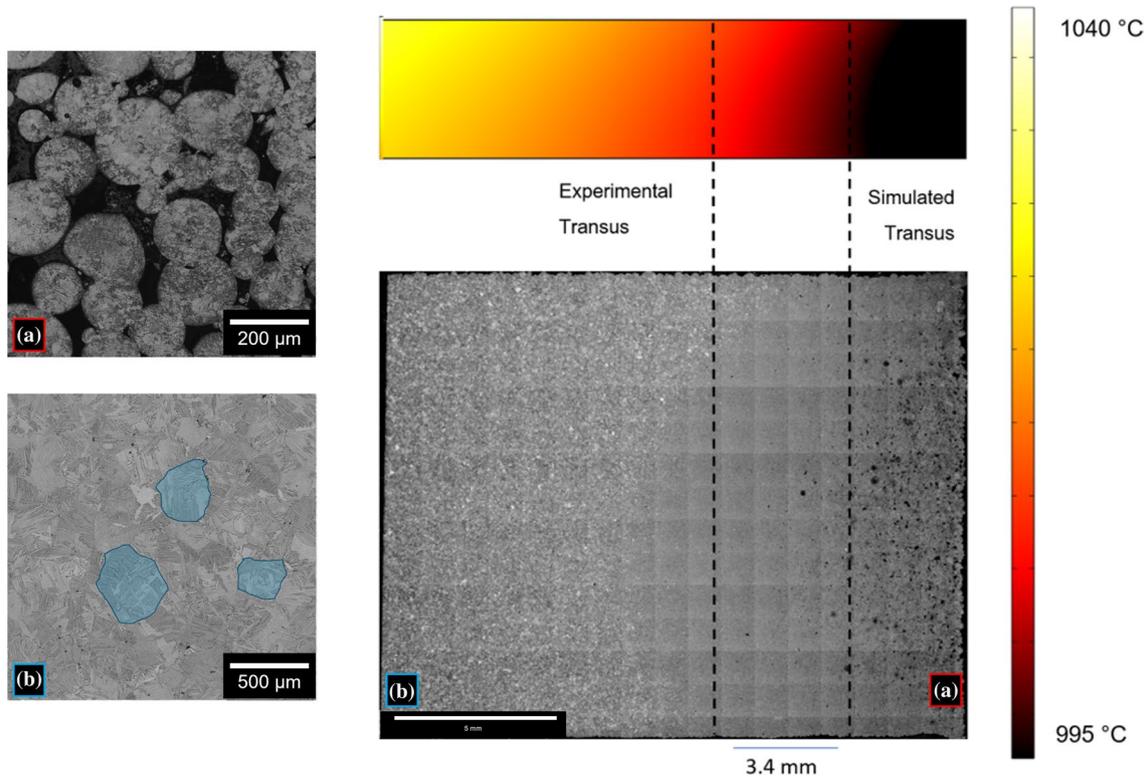
**Figure 6** Sample transus line separating equiaxed $\alpha$ particles (**A**) and prior $\beta$ regions (**B**) clearly visible on the etched Aperture sample (some examples highlighted) with a qualitatively similar angle. When measured it was found approximately 3 mm away from the predicted location providing an example of the potential accuracy of this prediction technique.

$\beta$ transus during processing and regions below the $\beta$ transus. Regions that experienced temperatures above the $\beta$ transus exhibit large $\beta$ grains due to the reduction in surrounding $\alpha$ phase to restrict grain growth due to the transformation from $\alpha$ to $\beta$ that occurs at and above this processing temperature. For the Aperture sample, the simulation predicted this feature at 19.5 mm from the edge, and in reality, it was measured to be 21 mm. A spatially resolved error range of ± 7% in this case, which is remarkably precise for this kind of application, especially as most industry applications would be this size or larger. This would imply that the expected 50 degrees gradient over the 20-mm length of the sample is also accurate, providing significant potential for control and prediction in future work. The relative homogeneity in the full sample when compared to the control samples also leaves much promise for the potential to reduce the issue of existing temperature gradients in large-scale production, maximising potential yield and minimising subsequent machining operations for a "right first time" approach.

For the samples with 5 min of dwell,[1] a significant increase in this average grain diameter was seen from the samples at 20 s dwell. With variations of over 100 $\mu m$ average grain diameter within a sample, the more subtle transitions in grain size due to temperature have become far clearer and may now be compared to the simulated values for more detailed validation of the predicted temperature profiles. For this analysis, the Olympus^{tm} microscope and Clemex^{tm} software were used to generate micrograph mosaics with individual images of increased magnification to examine the grains in more detail. These were run through a "recipe" generated in MIPAR which determined mean grain size through pixel count, and the resolution of images from the microscope. This "recipe" was a series of image refining steps attached to the tail end of the deep learning algorithm that were trained on other sample images from the same material system.

---

[1] Considered here to be a minimum for the practical use of this material to ensure full consolidation and grain growth.

**Figure 7** An overlay of the detected grains from a MIPAR processing step onto the original image displaying its effectiveness and accuracy (Top Right). The associated histogram of output data from the measurements is then a quantitative representation of the inset image, allowing us to output an average value and a range.
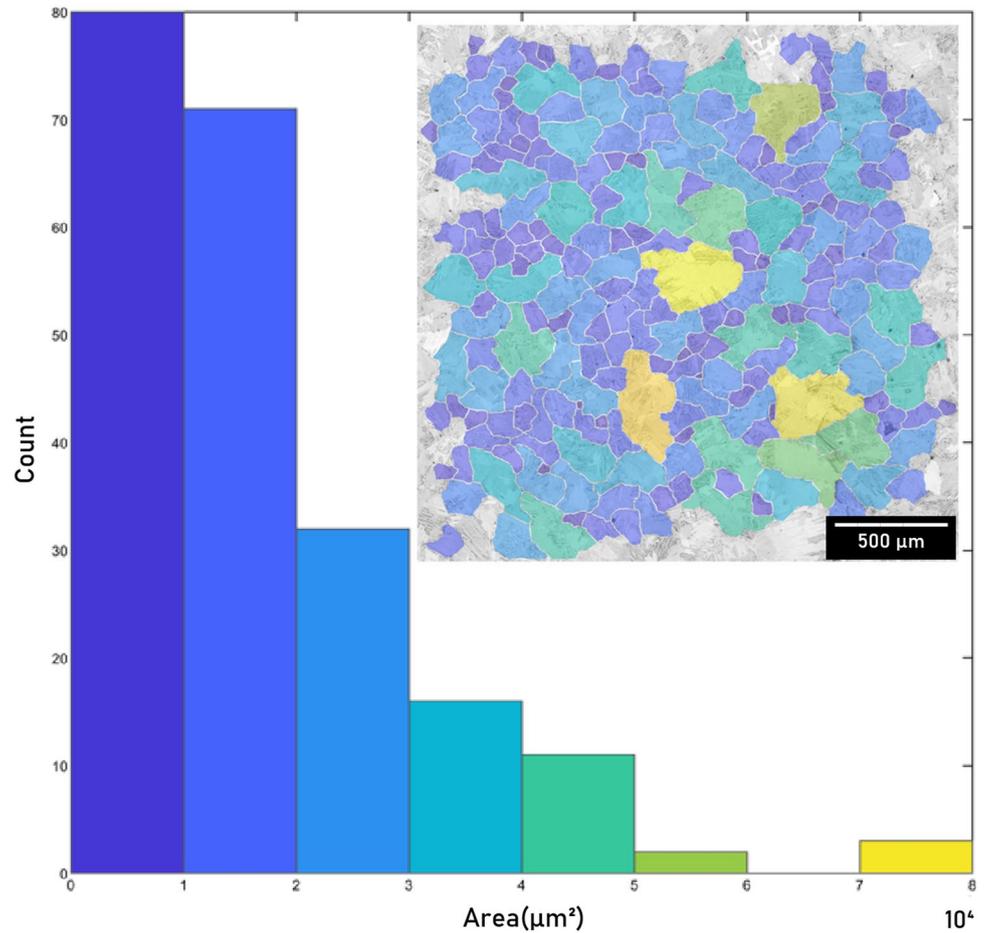


This histogram data were averaged, and the results plotted graphically for each micrograph in a grid with 1:1 representation to the fully imaged sample's mosaic structure. A script written in Python was then employed to plot the data and visually determine any trends and likenesses to predicted patterns from simulation.

Spherical grains were assumed for calculation purposes knowing that this would average out statistically for a large number of grains, though the compaction process deforms the initial spherical powder, visible in Fig. 7. Then, an average grain diameter was obtained for comparison to previous PSD where the particles were shown to be initially spherical as well as the sintered samples. As visible in Fig. 8, the raw data are difficult to visually parse through the noise. This noise is believed to be a statistical effect from the combination of slicing through randomly distributed planes of each three-dimensional grain, in addition to non-uniform grain growth during the sintering process. Therefore, a moderate Gaussian blur effect of

$\sigma^2 = 2$ within Python was also applied to more clearly define trends for direct visual comparison with simulated data. Further to this, the data were interpolated to a set of 1000 by 1000 points for smoothing of the resulting image. This trend analysis technique has not been carried forward in any quantitative work; however (as found in the previously cited work), the Gaussian blur has significant impact on the quantitative numerical outputs. It is in essence, a useful false colour image used for comparisons/validations with simulated temperature distributions.

## Final comparisons

As mentioned, during sample preparation, the 80-mm samples were cut into sections, resulting in some material loss, represented below with the white space between the samples. Additionally, during image analysis, part of these micrographs were cropped to avoid edge effects, accounting for the

**Figure 8** Top—A cropped micrograph containing stitched together higher resolution images in a mosaic from the Aperture Sample 5min Dwell. Bottom—Comparable MIPAR results plotted as raw data. Each square of the represented data displays the average diameter of the grains detected within that micrograph from the mosaic image above. This diameter is calculated assuming spherical grains.
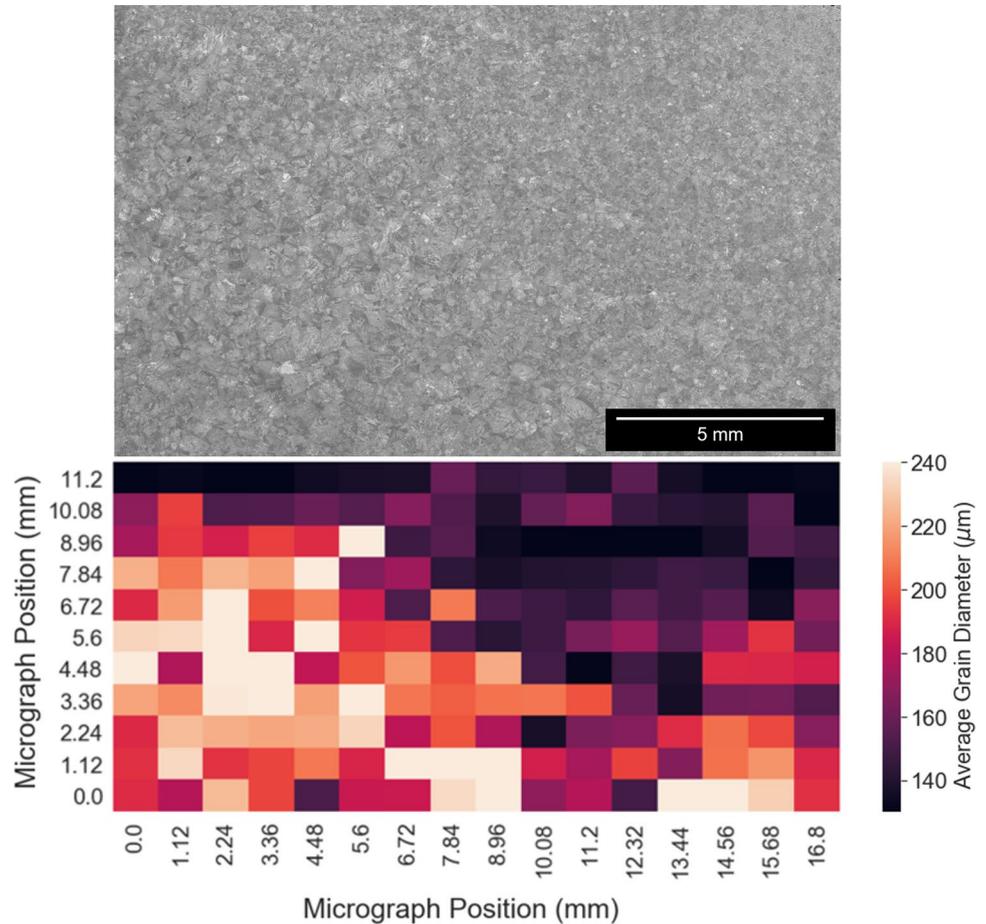


differences in scale. As such, in the qualitative comparison images of the four samples, the thermal distributions have also been appropriately cropped to match their practical counterparts. Figures 9, 10, 11 and 12 show the raw values of average grain diameter determined through the MIPAR deep learning above the processed images for comparison with the thermal distributions below. This allows us to qualitatively compare the effect of varying temperatures spatially on the resulting grain growth of the $\beta$ phase. It is expected that with greater available energy above the $\beta$ transus temperature, grains will show a corresponding increase in size. Some statistical variation is expected from two factors; the first being the distribution of grain sizes which naturally exist across a sample, and secondly, the influence of the cut depth. This references the location sectioned, and material ground during preparation, affecting the plane of the individual grain being sampled. The quantity of grains analysed has minimised some of this statistical variation, and for the purposes of

qualitative inspection, the image processing further reduces this factor.

This sample, prepared without any insulation, demonstrates a reasonably homogeneous outcome both in simulation and measured grain size. However, there is a region close to the edge (ii) where a lower grain size region is noticeable. Predicted to a very accurate degree by the simulated thermal profile (c), this region contains grains which are not significantly larger than the initial powder size distribution similarly to the 0 s dwell samples mentioned. This implies that the region only reached the transus temperature of 994 °C for a brief period in the 5 min dwell, possibly due to thermal overshooting caused by the high heating rate. Figure 9 also demonstrates the statistical variation discussed, especially in respect to the noise in the raw data (a) and the "hot spots" noticeable in the processed images as well as the original micrographs. This could be the result of some localised chemistry, potentially with a lower oxygen content reducing the $\beta$ transus slightly as oxygen is an $\alpha$ stabilising element
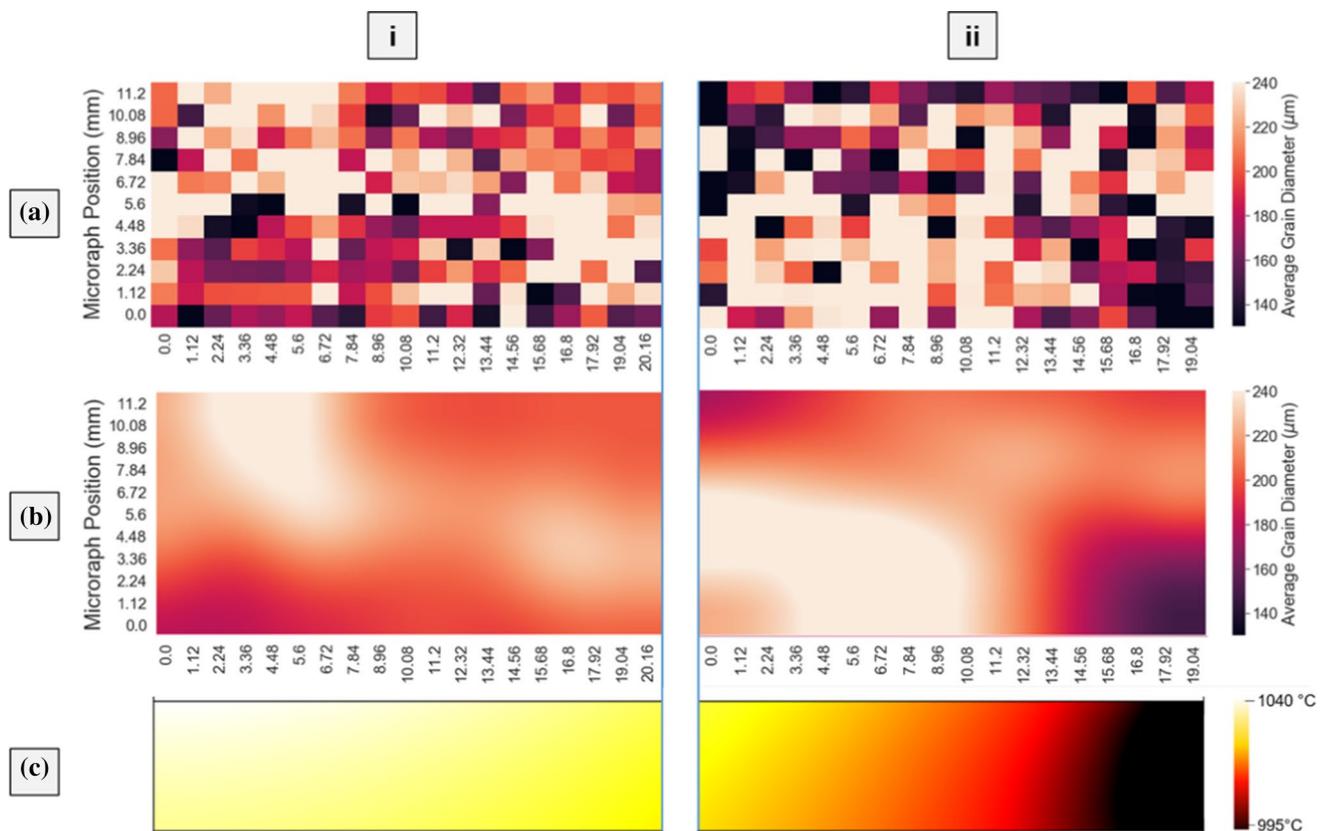
**Figure 9** Control (Sample centre left (i) and edge right (ii))- Raw (**a**) and processed (**b**) grain size distributions compared to the predicted temperature profiles (**c**) from Fig. 5 demonstrating the correlation between heating and resulting grain size. This

shows several unexpected spots of higher and lower grain size by approximately 30 $\mu$m but a very respectable overall agreement either side of the cut line from sample preparation.

and increases the $\beta$ transus. Additionally, it could be due to localised heating during early stages of the sinter causing early compaction, allowing more time for the grains to grow, unpinned by the particle boundaries. Overall, however, the trends show a remarkable degree of correlation and likely causation, demonstrating the predictive capabilities of the model.

When compared to the Control sample above, the Aperture sample, with insulation around the edge of the sample (ii) region depicted with inset B in Fig. 2 has a much more severe thermal gradient (c). This is caused when the insulation forces the current path to shift preferentially through the centre of the sample (i). Potentially increasing the current density in this region by up to a factor of four depending on the permeability of the BN layer. With this additional current, further Joule heating is expected and localised in the central region, and with the pyrometer measuring from a point closer to this area than the edge, the distribution becomes more severe. There are fewer "hot

spot" regions in this sample, implying a greater degree of homogeneity in this central heated region than the uninsulated sample provides from the concentrating of heating.

The reverse of the Aperture sample shows an interesting result that was initially unexpected. It is much colder than the other models and shows it with an average grain diameter 40–60 $\mu$m lower even in the higher temperature areas. This is somewhat unintuitive as it was thought that it would appear as an inverse of the Aperture result. However, from the simulation, it appears that the heating occurs primarily in the tooling on the side of the pyrometer. This heat travels through the tooling to the sample edge and pyrometer similarly quickly, and therefore, the heating will slow, or even stop when the desired temperature reaches both points. This will lower the sample's experienced temperature for an equivalent pyrometer reading to the other models as seen in the experimental results in Fig. 11. It demonstrates the importance of
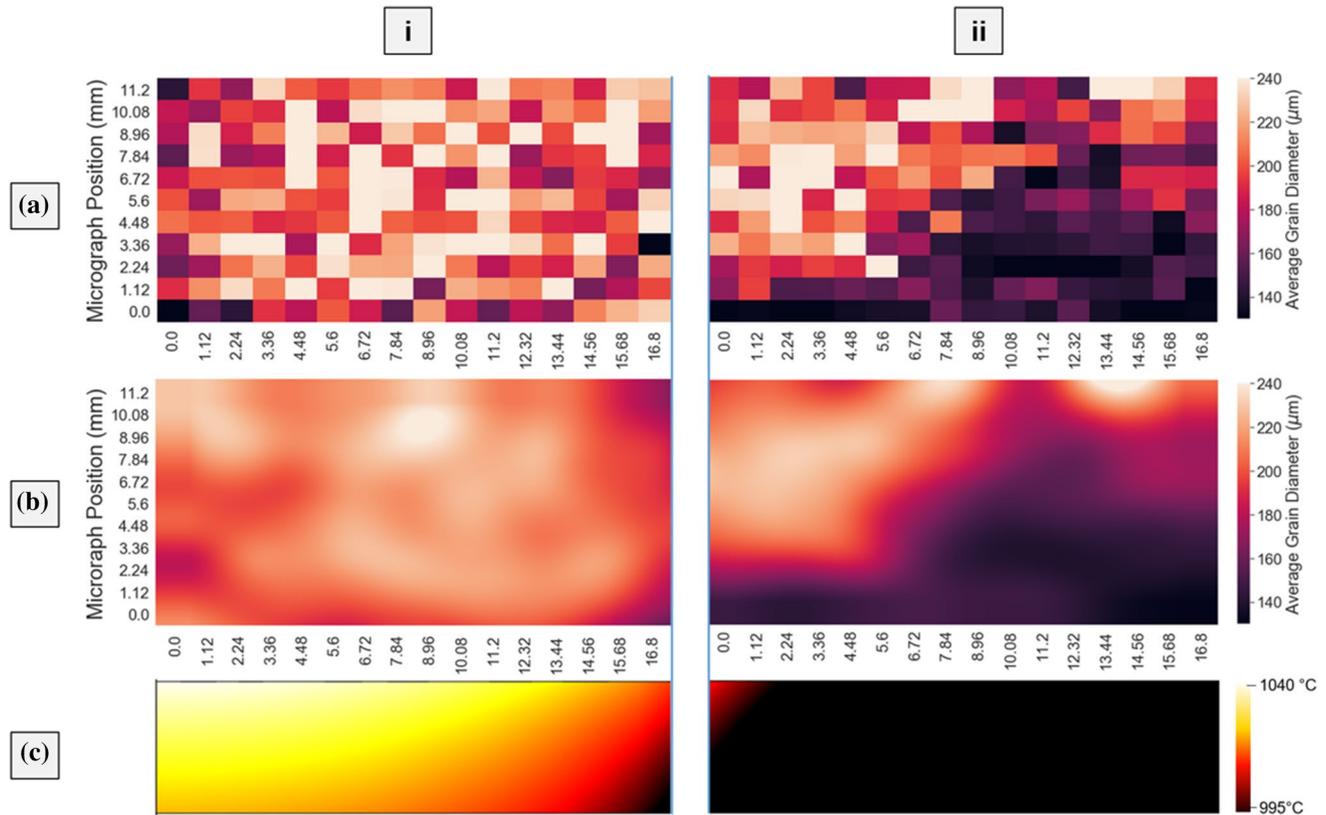
**Figure 10** Aperture (Sample centre left (i) and edge right (ii)- Raw (**a**) and processed (**b**) grain size distributions compared to the predicted temperature profiles (**c**) from Fig. 5 demonstrating the correlation between heating and resulting grain size. This shows a very accurate overall trend; however, the expected line of transus falls 7 mm short of its predicted location, likely due to thermal overshooting during which was noticed during the sintering run.

pyrometer location in relation to the direction of current flow and reveals interesting possibilities for this new variable using these insulation profiles.

For the final insulation profile, the overall temperature profile has completely reversed, with the centre (i) being at a lower heat than the edge (ii). It also seems the most homogeneous with respect to grain growth of the four samples even visible through the noise of the raw data (a). As visible here and in the other samples, the trends seen in the MIPAR data have a strong spatial correlation to the predicted thermal gradients across the samples with positional accuracy greater than initially hoped for on this 80-mm scale. These average grain sizes and their respective simulated temperatures can then be sampled to produce a quantitative graph of this correlation at these conditions. Looking at these values, it is possible to compare them to previous studies by Semiatin et al. [41] where for powder with initial diameter of 40 $\mu$m, prior $\beta$ grain diameters of between 200 and 300$\mu$m were found for

peak times and temperatures only 20 °C higher than those reported here. Although no lower temperatures were examined in these works, this quantitative match provides additional support for the findings. It should be noted though that this graph is limited to this material system, processed under super-transus conditions with similar $\alpha$–$\beta$ chemistry. Although this limits the broader impact, it still maintains great utility for further work and for similar systems. It also demonstrates possibilities for its application in an industrial setting where similar materials systems are used regularly, and optimisations are impactful.

Although it was most obvious in the Reverse sample, all the samples also demonstrated some sensitivity to the direction of current flow and pyrometer position with the upwards facing gradient of their $\beta$ transus angle, red to black transition. This is as thermal equilibrium of the system varies depending on the insulation profile, the actual temperatures reached within the sample depend on the
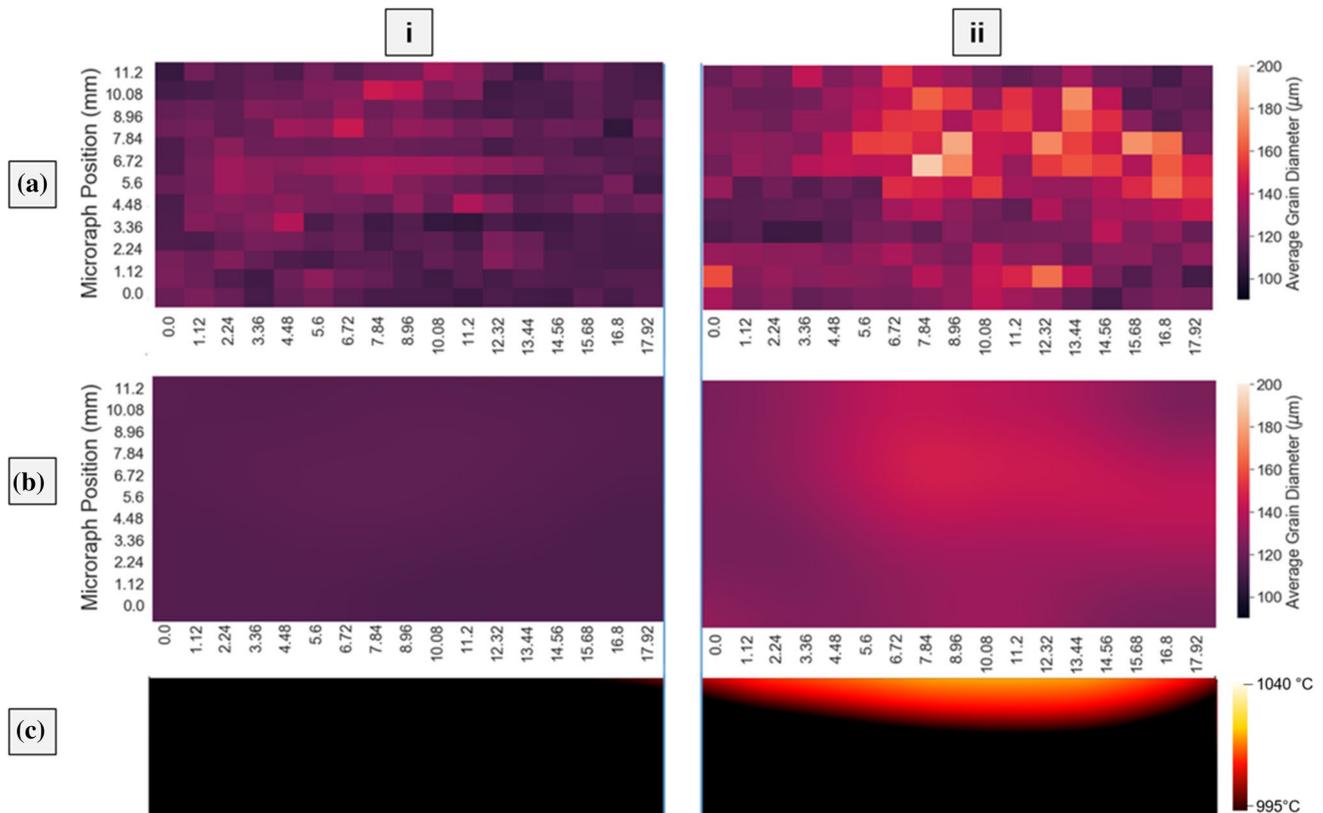
**Figure 11** Reverse Aperture (Sample centre left (**i**) and edge right (**ii**)-Raw (**a**) and processed (**b**) grain size distributions compared to the predicted temperature profiles (**c**) from Fig. 5 demonstrating the correlation between heating and resulting grain size. This accurately predicted the temperatures being too low to cause significant grain growth in the majority of the sample, in addition to the region and trend line of mild increase. A region in the centre, however, is still super-transus and so the thermal profile is potentially a little cold overall, again due to thermal overshoot during sample creation.

recipe, controlled by the pyrometer. If the pyrometer is measuring from a region where the thermal distribution is colder, then the average temperature in the hotter regions will be higher and vice versa; this is an issue with both thermocouple control and surface pyrometers which may be remedied with some simulated knowledge of the internal system. This correlation is important, as with different geometries it could lead to unexpected gradients at the process scales in complexity. This will be important to consider going forwards as a qualitative observation, but more quantitative results are possible here too.

The plot above is simply generated from a direct quantitative comparison of pseudo-randomly sampled points from all four tests (Fig. 9, 10, 11, 12, 13), and shows strong predictability using this technique. It can certainly be said that it has a clear visible correlation, and with an $R^2$ value of 0.75, it shows a quantifiable

trend within this dwelling period. It also makes an obvious case for this analysis route to be tested further on other systems, and through other processing/sintering conditions. In future work, this process can be further tuned, and a solid predictive tool generated to advance the "right first time" approach which has recently become so sought after in powder processing, and specifically SPS/FAST. For example, with a different sample size, or insulation profile, a new thermal gradient can be simulated. Then, in advance of creating the sample, this gradient can be adjusted such that the temperatures, and thus grain size distributions, fit the desired outcomes.

One such example is with the scaling of the technique, not only in diameter, but also in height. As is visible even in these samples of 20-mm thickness, there is some thermal gradient in the Z-axis in addition to that in R. This is an issue which scales problematically with size requiring significantly more energy
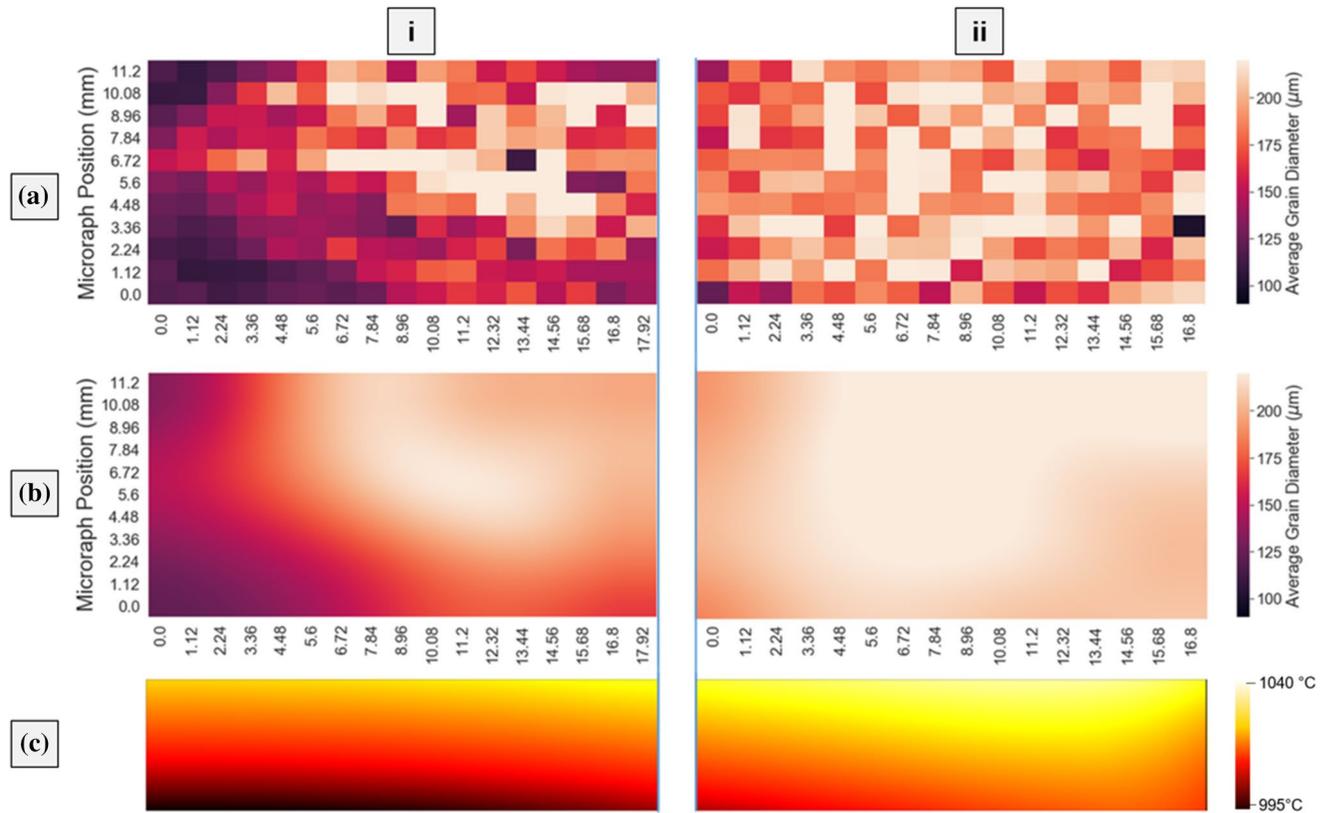
**Figure 12** Full (Sample centre left (i) and edge right (ii)-Raw (**a**) and processed (**b**) grain size distributions compared to the predicted temperature profiles (**c**) from Fig. 5 demonstrating the correlation between heating and resulting grain size. The trend line again appears to fit the profile very well with the most seemingly homogenous large grain growth out of the sample edges.



**Figure 13** Ti-6Al-4V sintered super-transus grain growth plotted as average grain size against highest predicted temperature for a 5 min dwell. The sampling was done pseudo-randomly and shows a good fit linear trend which would be interesting to test the boundaries of in further experimentation.
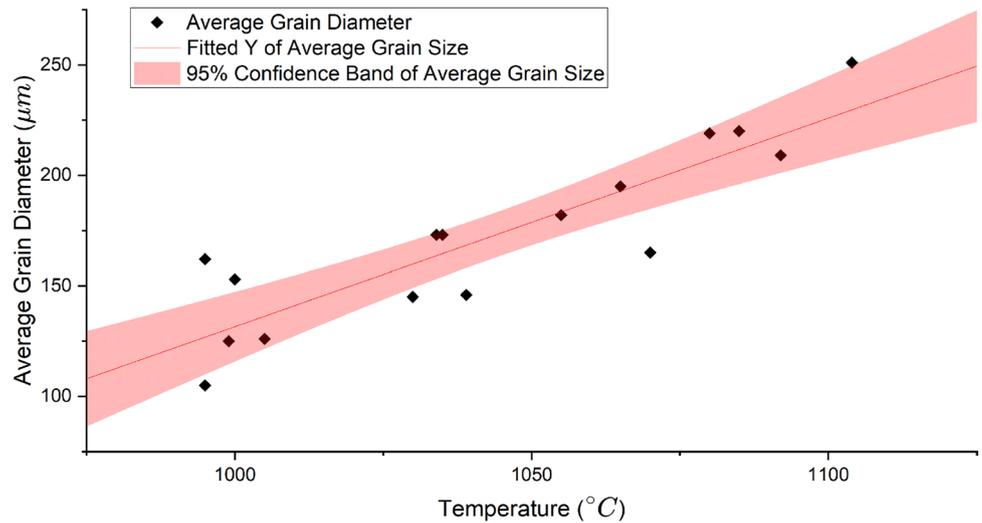
than previously to reach desired temperatures and occasionally causing undesirable microstructures to form. It is hoped that with simulations like this and a database of grain growth information, it will be possible to minimise, or even remove these gradients in some cases, before the sample is even created. This

would result in the saving of significant quantities of material, time, and energy at scales larger than that of a laboratory.

It is likely that for this purpose, an energy map, in addition to this temperature plot in Fig. 13, based on the power and time used in the dwell period of the sinter, could be of sufficiently broad use but was not within the scope of the work here. Certainly, if a larger range of sizes and temperatures is investigated in future to ascertain a more definitively widely applicable grain size prediction tool, a map of this nature would be invaluable. Additionally, some small-scale particle simulation or a grain growth model could be created for further validation and predictive capability, and both ideas are strongly recommended for future efforts.

## Conclusions

An expansion on a previously under explored technique for FAST processing has been tested on a common titanium alloy to examine the potential for impact and control over the final microstructure in a single step process. It has been shown that with the help of an accompanying FEM simulation, remarkable thermal gradients of over 100 °C are possible and designable, even within the relatively small scale of an 80-mm test sample. The analysis of this revealed that prediction and spatial control of the final microstructure is resolved down to a few millimetres, with the size of grains produced being predictable within a defined error range provided some previous knowledge for the material system. With this technique, it may also be possible to sinter dissimilar materials more easily with varying consolidation points, or perhaps design and create non-homogeneous microstructures to suit a pre-specified function. Perhaps more simply, and excitingly for the industry which has recently shown more interest in this technique, it also holds great potential to balance any concerns with thermal gradients and increase homogeneity in samples greater in scale. With minimal addition to the existing process, increasing the yield efficiency of the powder to create useful material prior to further processing is possible.

Additionally, with the Reverse sample, an important feature of the process, in the location of a pyrometer in relation to the flow of current, was highlighted for its impact on resulting thermal gradients. It has been noted from the model that this is likely to become significantly more prevalent for larger-scale samples in future.

Finally, the use of MIPAR for the purpose of analysing titanium super-transus prior $\beta$ grains has been demonstrated, along with its utility for obtaining information of this kind on a large scale. This allows for potential further scaling of this analytical technique for spatial resolution to the largest samples currently producible, at 250 mm diameter, with much less effort than a manual approach would require. It also will allow for the measurement, and therefore, potential control of the Ti-6Al-4V $\alpha$ microstructures which are the most sought after for operational components in aerospace provided sufficient resolution on the mosaic micrography. There is also potential for this technique and the level of control it can provide to be useful for material systems without solid-state transformations such as seen here or those of mixed composites. Some examples provided here include the Ti-TiB system for ballistic applications or for the creation of designed porosity for functionally graded properties in metal or ceramic systems.

## Acknowledgements

## Author contributions

OLB provided valuable early insights on the thermal gradients in sintering and assisted in the creation of the MIPAR deep learning model and recipe. BT greatly assisted with the initial creation of the COMSOL simulation and provided feedback on early iterations of the FAST sintering samples. MJ advised on the microstructural aspects of titanium processing as well as the composition of the manuscript.

## Declarations

**Conflicts of interest** There are no known conflicts of interest for this work.

## References

[1] M. Shahedi Asl, Z. Ahmadi, A. Sabahi Namini, A. Babapoor, and A. Motallebzadeh, "Spark plasma sintering of tic-sicw ceramics," Ceramics International, vol. 45, no. 16, pp. 19 808–19 821, 2019. [Online]. Available: https://www.sciencedirect.com/science/article/pii/S0272884219317377

[2] B. Niu, F. Zhang, J. Zhang, W. Ji, W. Wang, and Z. Fu, "Ultra-fast densification of boron carbide by flash spark plasma sintering," Scripta Materialia, vol. 116, pp. 127–130, apr 2016. [Online]. Available: https://www.sciencedirect.com/science/article/pii/S1359646216300562

[3] E. Calvert, A. Knowles, J. Pope, D. Dye, and M. Jackson, "Novel high strength titanium-titanium composites produced using field-assisted sintering technology (fast)," Scripta Materialia, vol. 159, pp. 51–57, 2019. [Online]. Available: https://www.sciencedirect.com/science/article/pii/S1359646218305128

[4] Z. Trzaska, C. Collard, L. Durand, A. Couret, J.-M. Chaix, G. Fantozzi, and J.-P. Monchoux, "Spark plasma sintering microscopic mechanisms of metallic systems: Experiments and simulations," Journal of the American Ceramic Society, vol. 102, no. 2, pp. 654–661, 2019. [Online]. Available: https://ceramics.onlinelibrary.wiley.com/doi/abs/10.1111/jace.15999

[5] M. Abedi, S. Sovizi, A. Azarniya, D. Giuntini, M. E. Seraji, H. R. M. Hosseini, C. Amutha, S. Ramakrishna, and A. Mukasyan, "An analytical review on spark plasma sintering of metals and alloys: from processing window, phase transformation, and property perspective," Critical Reviews in Solid State and Materials Sciences, vol. 0, no. 0, pp. 1–46, 2022. [Online]. Available: https://doi.org/10.1080/10408436.2022.2049441

[6] Voisin T, Monchoux JP, Durand L, Karnatak N, Thomas M, Couret A (2015) "An Innovative Way to Produce γ-TiAl Blades: Spark Plasma Sintering," Advanced Engineering Materials, **17**(10), 1408–1413, , cited By 11. [Online]. Available: https://hal.science/hal-01726307

[7] Delaizir G, Bernard-Granger G, Monnier J, Grodzki R, Kim-Hak O, Szkutnik P-D, Soulier M, Saunier S, Goeuriot D, Rouleau O, Simon J, Godart C, Navone C (2012) A comparative study of spark plasma sintering (sps), hot isostatic pressing (hip) and microwaves sintering techniques on p-type bi2te3 thermoelectric properties. Mater Res Bull 47(8):1954–1960

[8] Macía E, García-Junceda A, Serrano M, Hernández-Mayoral M, Diaz L, Campos M (2019) Effect of the heating rate on the microstructure of a ferritic ods steel with four oxide formers (y-ti-al-zr) consolidated by spark plasma sintering (sps). J Nuclear Mater 518:190–201

[9] Zapata-Solvas E, Gómez-García D, Domínguez-Rodríguez A, Todd RI (2015) Ultra-fast and energy-efficient sintering of ceramics by electric current concentration. Sci Rep 5:1–7

[10] Lee G, Manière C, McKittrick J, Olevsky EA (2019) Electric current effects in spark plasma sintering: From the evidence of physical phenomenon to constitutive equation formulation. Scrip Mater 170:90–94

[11] Manière C, Nigito E, Durand L, Weibel A, Beynet Y, Estournès C (2017) Spark plasma sintering and complex shapes: the deformed interfaces approach. Powder Technol 320:340–345

[12] Manière C, Torresani E, Olevsky EA (2019) Simultaneous spark plasma sintering of multiple complex shapes. Materials 12(2):1–14

[13] Mouritz AP, Introduction to aerospace materials. Elsevier, (2012)

[14] Lütjering G, Williams JC (2007) Titanium matrix composites. Springer,

[15] Leyens C, Peters M (2003) Titanium and titanium alloys: fundamentals and applications. Wiley, NJ

[16] Weston NS, Derguti F, Tudball A, Jackson M (2015) Spark plasma sintering of commercial and development titanium alloy powders. J Mater Sci 50:4860–4878

[17] Guillon O, Gonzalez-Julian J, Dargatz B, Kessel T, Schierning G, Räthel J, Herrmann M (2014) Field-assisted sintering technology/spark plasma sintering: mechanisms, materials, and technology developments. Adv Eng Mater 16(7):830–849

[18] Hu Z-Y, Zhang Z-H, Cheng X-W, Wang F-C, Zhang Y-F, Li S-L (2020) A review of multi-physical fields induced phenomena and effects in spark plasma sintering: fundamentals and applications. Mater Des 191:108662

[19] Weston NS, Jackson M (2020) Fast-forge of titanium alloy swarf: a solid-state closed-loop recycling approach for aerospace machining waste. Metals 10(2):296

[20] Garay JE (2010) Current-activated, pressure-assisted densification of materials. Ann Rev Mater Res 40:445–468

[21] Kelly JP, Graeve OA (2015) Spark plasma sintering as an approach to manufacture bulk materials: feasibility and cost savings. Jom 67(1):29–33

[22] Manière C, Durand L, Brisson E, Desplats H, Carré P, Rogeon P, Estournès C (2017) Contact resistances in spark plasma sintering: from in-situ and ex-situ determinations to an extended model for the scale up of the process. J Europ Ceram Soc 37(4):1593–1605

[23] Eriksson M, Zz Shen, Nygren M (2005) Fast densification and deformation of titanium powder. Powder Metall 48:231–236

[24] Wang D, Yuan H, Qiang J (2017) The microstructure evolution, mechanical properties and densification mechanism of Tial-based alloys prepared by spark plasma sintering. Metals 7(6):201

[25] Li X, Yang C, Lu H, Luo X, Li Y, Ivasishin O (2019) Correlation between atomic diffusivity and densification mechanism during spark plasma sintering of titanium alloy powders. J Alloys Compd 787:112–122

[26] Xie S, Li R, Yuan T, Zhang M, Wang M, Wu H, Zeng F (2018) Viscous flow activation energy adaptation by isothermal spark plasma sintering applied with different current mode. Scr Mater 149:125–128

[27] Trzaska Z, Bonnefont G, Fantozzi G, Monchoux JP (2017) Comparison of densification kinetics of a tial powder by spark plasma sintering and hot pressing. Acta Mater 135:1–13

[28] Yang C, Zhu M, Luo X, Liu L, Zhang W, Long Y, Xiao Z, Fu Z, Zhang L, Lavernia E (2017) Influence of powder properties on densification mechanism during spark plasma sintering''. Scr Mater 139:96–99

[29] Vanmeensel K, Laptev A, Hennicke J, Vleugels J, Van der Biest O (2005) Modelling of the temperature distribution during field assisted sintering. Acta Mater 53(16):4379–4388

[30] Li S, Liu Y, Sun F, Fang H (2021) Multi-particle molecular dynamics simulation: shell thickness effects on sintering process of cu-ag core-shell nanoparticles. J Nanopart Res 23:1–4

[31] Olevsky EA, Tikare V, Garino T (2006) Multi-scale study of sintering: a review. J Am Ceram Soc 89(6):1914–1922

[32] Multiphysics C (1998) Introduction to comsol multiphysics®. COMSOL Multiphysics, Burlington, MA, accessed **9**(2018): 32

[33] Dickinson EJ, Ekström H, Fontes E (2014) Comsol multiphysics ®: finite element software for electrochemical analysis. a mini-review. Electrochem Communi 40:71–74

[34] Wang C, Cheng L, Zhao Z (2010) Fem analysis of the temperature and stress distribution in spark plasma sintering: modelling and experimental validation. Computat Mater Sci 49(2):351–362

[35] Olevsky EA, Garcia-Cardona C, Bradbury WL, Haines CD, Martin DG, Kapoor D (2012) Fundamental aspects of spark plasma sintering: II. Finite element analysis of scalability. J Am Ceram Soc 95(8):2414–2422

[36] Manière C, Pavia A, Durand L, Chevallier G, Afanga K, Estournès C (2016) Finite-element modeling of the electro-thermal contacts in the spark plasma sintering process. J Europ Ceram Soc 36(3):741–748

[37] Levano Blanch O, Lunt D, Baxter GJ, Jackson M (2021) Deformation behaviour of a fast diffusion bond processed from dissimilar titanium alloy powders. Metall Mater Trans A 52(7):3064–3082

[38] Sosa J, Huber D, Welk B, Fraser H (2017) Mipar$^{Tm}$: 2d and 3d image analysis software designed by materials scientists, for all scientists. Microsc Microanal 23(S1):230–231

[39] Fu Z, Freihart M, Wahl L, Fey T, Greil P, Travitzky N (2017) Micro-and macroscopic design of alumina ceramics by robocasting. J Europ Ceram Soc 37(9):3115–3124

[40] Zhang H, Xiong J, Guo Z, Yang T, Liu J, Hua T (2021) Microstructure, mechanical properties, and cutting performances of wc-co cemented carbides with ru additions. Ceram Int 47(18):26050–26062

[41] Semiatin S, Soper J, Sukonnik I (1996) Short-time beta grain growth kinetics for a conventional titanium alloy. Acta Mater 44(5):1979–1986

**Publisher's Note** Springer Nature remains neutral with regard to jurisdictional claims in published maps and institutional affiliations.